ORIGINAL ARTICLE

I|J|A|M|B JOURNALAMB.COM
INTERNATIONAL JOURNAL OF ADVANCES IN MEDICAL BIOTECHNOLOGY

Characterization of 3D-Printed β-TCP Scaffolds with Enhanced Microstructure, Mechanical Properties, and Cell Compatibility

G.H.M. Gomes[1]; J. K.M.B.Daguano[2];J.G.Bastidas[2]; K.N. Ferreira[3]; P.H.J.O.Limirio[4]; P.Dechichi[4]; L.E.Carneiro-Campos[5]

*Corresponding author: E-mail address: gustavohmg@unifei.edu.br

Received: October 2024; Accepted: December 2024.

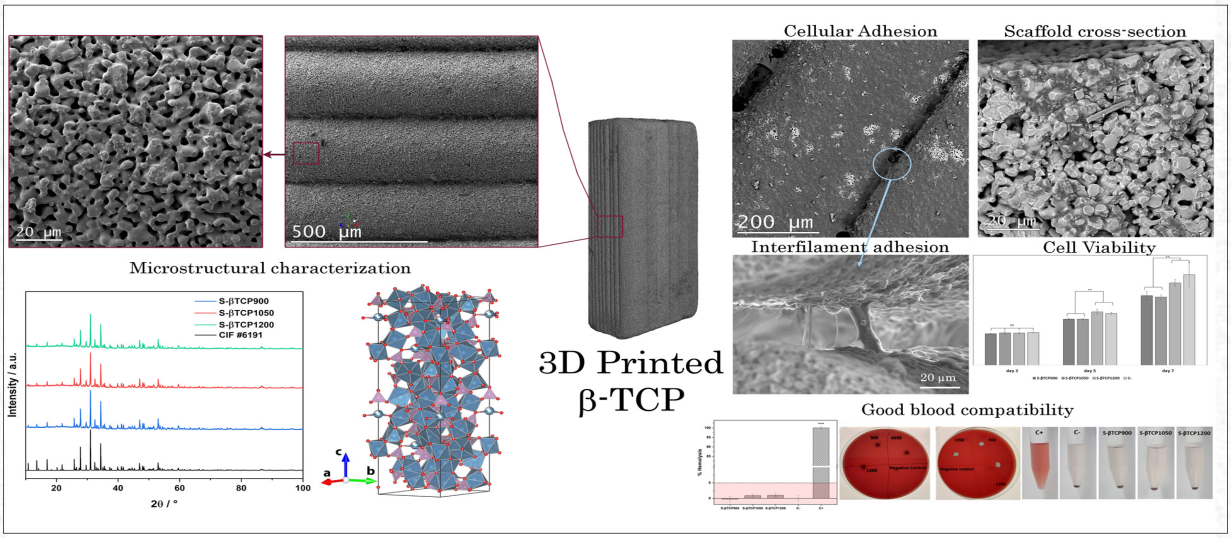

Abstract: Achieving bone regeneration in large defects caused by trauma, pathology and atrophy is a challenge. Innovative implant materials are emerging as alternatives to autografts in regenerative medicine. 3D-printed β-tricalcium phosphate (β-TCP) scaffolds have emerged as a promising solution for bone tissue replacement, offering patient-specific implants without relying on donors or transplantation. There are many open questions that need to be addressed before they can be used on a large scale. The analysis of sintering temperatures and the different crystalline phases, the in-depth evaluation of the microstructure and its biological response, as well as the assessment of suitable mechanical properties are some of these. The present study carried out a comprehensive characterization of the microstructure of commercial 3D-printed β-TCP using X-ray diffraction coupled with Rietveld refinement, X-ray microtomography and scanning electron microscopy. In addition, blood and cell compatibility tests were carried out using MG63 cells. The imaging techniques revealed the influence of the sintering treatment on the microstructure, resulting in an increase in the average pore size, efficient coalescence between particles and a shrinkage effect at higher temperatures. This behavior had a direct impact on the mechanical properties and cell adhesion behavior. Blood compatibility showed no significant differences between all the samples. However, the material sintered at 1200 °C showed better mechanical properties and a better behavior in the adhesion and proliferation of MG63, which were correlated with a higher density, improved mechanical properties and interconnected porosity, which play a key role in improving osteoblastic function.

Keywords: Tricalcium phosphate. Scaffolds. Additive manufacturing. 3D-printing. Structural characterization.

---

[1]Institute of Pure and Applied Sciences, Federal University of Itajubá, Itabira, MG, Brazil.
[2]Center of Information Technology Renato Archer, Campinas, SP, Brazil.
[3]University of São Paulo, Pirassununga, Brazil.
[4]Federal University of Uberlândia, Brazil.
[5]Fluminense Federal University, Innovation Agency, Brazil.

https://doi.org/10.52466/ijamb.v6i2.131

Introduction

Medical complications due to trauma, pathology, and bone atrophy are challenges for surgical reconstructions and tissue recovery in cases of extensive damage (critical-size defects)[1]. The need for the development of technologies that can reduce the number of surgeries, morbidity, and cost is still an open question[2].

For many years, the use of autogenous bone tissue remains as gold standard for cranio-maxillo-facial, orthopedic, and dental implant reconstructions[3]. However, it is usually associated with morbidity, aesthetic, and functional complications[4].

Macroscopically, bone tissue is made up of two parts: cortical and cancellous bone. The cortical bone is highly dense and is responsible for providing the primary mechanical properties of bone. Its nutrition is ensured by an intricate number of channels containing blood vessels distributed longitudinally and transversely (Haversian canals and Volkmann canals), connected to the inner and outer surfaces of the cortical structure[5-7]. Cancellous bone is directly immersed in the bone marrow stroma and is composed of several intertwined trabeculae providing sufficient space for the development of bone cells and vascular networks[8]. Moreover, 80% of the bone remodeling processes during life occur in this region[9].

In recent decades, interest has arisen in bioengineered implants as reliable alternatives to autografts for the recovery of extensive bone damage. Advances in materials and computerized solutions have made it relatively simple to convert tomographic images into implantable scaffolds for bone reconstruction[10,11]. The technique enables the precise fabrication of customized patient-specific solutions without relying on donor sites or transplantations[12]. In this scenario, synthetic 3D-printed bioceramic scaffolds have emerged as viable solutions due to their osteoconductive capacity for bone engineering. The main advantageous features of these biomaterials are: optimized mechanical properties, plasticity, and controlled degradation. In addition, its alloplastic condition does not demonstrate antigenic effects, the possibility of disease transmission, or any other relevant issue to consider[13,14].

To achieve the success of 3D-print scaffolds for bone repair, many factors are required, such as physical and chemical characteristics. In addition, the precision of the manufacturing process to produce robust, high-resolution implants is necessary for the stable formation of the bone-implant interface[15]. In order, to obtain an accurate response, the scaffolds must be designed to mimic living tissue, improving blood circulation, and cell colonization, and facilitating the process of bone formation[16,17].

The use of 3-D printing technologies for bones[18,19] and cartilage regeneration are being approached, with good results, using acellular porous scaffolds that do not seem to induce persistent inflammation or an active immune response[20-22]. Among these materials, ceramic composites are the most studied for the development of biofabricated scaffolds for bone engineering, due to the similarity to natural apatites of bone matrix[23,24]. Due to its osteoconduction capacity, β-tricalcium phosphate (β-TCP) bioceramic has been widely tested as an option for critical-size bone defects[25]. Even under these conditions, bone remodeling is known to be a complex and highly regulated process. Different molecular activations that control its initiation, progression, and quiescence are still not fully understood[26]. To achieve this, inks for 3D printing must align not only with biocompatibility but also with printability, which is not easy. For example, thermoplastic inks' high melting temperatures used in traditional 3D printing are a challenge to overcome[27]. High temperatures result in the formation of secondary phases and highly crystalline surfaces, while lower temperatures diminish bending strength and the arrangement of the material particles, thereby limiting native cells and local response for bone regeneration[28,29]. Recognizing the physicochemical processes and their relevance in the crystal arrangement of the biomimetic calcified matrix, transcribing this information to the signaling network of gene activation, and triggering a remodeling process is what is expected when alloplastic graft materials are used[30].

Bioceramic inks, incorporating β-TCP and fatty acids, have been successfully used in the development of 3D printing scaffolds. The remodeling capacity and regeneration of native bone have been demonstrated *in vivo* models[29]. Slots *et al.* showed that these scaffolds retained their pre-sintering shape and chemical composition after sintering, exhibiting clinically relevant mechanical strength[31]. However, dimensional instability caused by sintering shrinkage is a drawback in bioceramics processing, along with limited dissolution in the body environment [32].

The interest increases in the β-TCP scaffolds promoted the arising of several commercial companies, commercializing ready-to-use scaffolds for bone regeneration. For example, the product MyBoneR© (CERHUM company) has recently shown improved bone regeneration capability in large animal models employing 3D gyroid-shaped scaffolds, demonstrating the absence of toxicity and no side effects on the sheep implant in the femur, demonstrating good reliability when compared with Bio-Oss® bovine standard, readily employed in the literature[33]. T&R Biofab also produces polycaprolactone and β-TCP scaffolds and has demonstrated efficient biocompatibility, osteoinductivity, and osteoconductivity[34]. Ossiform® ApS (Denmark) also produces high-quality β-TCP/fatty acid scaffolds, as green pieces. A recent paper by the company shows that 3D-printed β-TCP scaffolds led to the replacement of vascularized compact bone after six months in mini pigs, leading to excellent osteointegration, with no immune reaction[35]. However, despite the advances, there are still concerns about the microstructure and the functionality of those employed materials, even by commercialized products. A better understanding of the porosity, mass transfer, and how microstructural properties affect their biocompatibility are largely necessary [36]. A work by Podgórski et al. showed the importance of tailoring the scaffold's porosity, even using fatty acids and organic content that can act as porogenic agents, leading to an internal structure with connected pores [37]. Another work by Slavin et al. showed that lower sintering temperatures (~ 600 °C) lead to high cellular stress, contraly, scaffolds sintered at high temperatures (~1100 °C) showed a morphological change in the particle size and porosity, also leading to improved cellular response, showing only a small amount of cellular stress instances. However, the sintering process at higher temperatures also caused crystal phase transformation, probably leading to the observed instances of acute cellular stress [38].

In this sense, this work aims to enhance the understanding of how the physicochemical features of β-TCP 3D-printed scaffolds influence the bone microenvironment. The study employs imaging techniques such as scanning electron microscopy (SEM) and X-ray microtomography (μCT) to understand how the sintering process affects the total porosity, filament thickness, shrinking process, and mineral density of the scaffolds, compared with the performed mechanical analysis. Moreover, hemocompatibility and biocompatibility tests with MG63 were carried out to understand its biological behavior.

Materials and Methods

In this study, fabricated β-Tricalcium Phosphate (β-TCP) Ossiform™ scaffolds, from Odense, Denmark were used. Twelve rectangular bars (25.0 mm long, 2.0 mm wide, and 2.0 mm thick) and twelve gyroid-shaped discs (6.0 mm in diameter and 2.0 mm in width) were checked using a Digimatic caliper (Mitutoyo Absolute Digimatic Caliper, Tokyo, Japan). The samples were prepared using a β-TCP powder with stearic acid to form a paste, then the ink was transferred to a syringe and the scaffolds were printed using an extrusion process. More information about the methodology used by Ossiform™ can be found in previous papers[25,31,35]. The pre-sintering stage was carried out for 1 hour at 400 °C, with a cooldown of 2h before sintering. Then, the samples were sintered at 900, 1050, and 1200 °C in triplicate, in atmospheric air, for 16 hours. The samples were named S-βTCP900, S-βTCP1050, and S-βTCP1200, respectively.

X-ray diffraction (XRD) and Rietveld analysis

X-ray diffraction analysis was conducted to determine the crystalline phase of the samples, using a SHIMADZU 7000 with a theta-2theta configuration, Cu radiation ($K\alpha$ = 1.5406 Å) with a voltage of 40 kV and a current of 30 mA. A divergence and scatter slit of 1.00°, with a step size of 0.02°, collection time of 1.2s, and a 2θ range of 10° – 100°. The Rietveld refinement analysis was performed using the GSAS/EXPGUI free software[39] and the standard Crystallographic Information File (CIF) from ICSD with code #6191. This analysis aimed to obtain information on the $Ca_3(PO_4)_2$ crystal structure, including phase, lattice parameters, calculated density, occupation of Ca(4) site, and position of atoms in the lattice. The VESTA software was used for structure visualization and plotting[40].

FTIR functional group analysis

The identification of functional groups in the samples was carried out using Fourier transform infrared (FTIR) analysis on a Perkin Elmer Infrared Spectrometer Spectrum 100. The FTIR scans covered a range of 400-4000 cm^{-1} wavenumber, and an average of 16 scans were recorded with a spectral resolution of 4 cm^{-1}, using attenuated total reflectance (ATR) mode. This method allowed for the precise identification of functional groups present in the samples.

Scanning electron microscopy (SEM)

The scanning electron microscopy (SEM) analysis was carried out in a FEG-SEM TESCAN MIRA3 XMU equipment employing the secondary electron (SE) detector at an acceleration voltage of 1.5 kV, with a spot size of 5.2 nm, and ultra-high vacuum (UHV). The tree samples in the study were analyzed on a top view of the printed filament, a close view of the particles on the top, and the fracture of the materials. All the samples were coated with gold nanoparticles to avoid charging effects. The equipment employed for the gold coating is a Sputter Coater from BALTEC, model BALZERS – SCD 050, with the parameters of 50 mA of current, sputtering time of 30 seconds, and 0.05 mbar of working pressure, leading to a 10 nm gold deposition film.

X-Ray microtomography

To investigate the sintering process of 3D-printed scaffolds and determine porosity parameters, X-ray microtomography (μCT) was employed. The SKYSCAN 1272 CMOS Edition from Bruker was used for all sample imaging, and images were acquired under consistent conditions. The acquisition parameters for the 2048 x 2048 pixel image included flat field correction, a 6 μm pixel size, a Cu 0.11 mm filter, a 16-megapixel camera detector, random movement of 50 pixels, an exposure time of 1073 ms, a voltage of 100 kV, a current of 100 μA, four-frame averaging, and a rotation step of 0.4° with a half-rotation of 180°. Standard procedures were followed to obtain images free of digital artifacts. Reconstruction and visualization of the 3D images were performed using NRecon and CTVox software provided by Bruker. The Results and Discussion section provides further details regarding the reconstruction methodology. The porosity, pore size distribution, and filament thickness values were obtained using the CTan software. The methodology employed the following steps: Filtering with Anisotropic diffusion in the 2D space with 10 iterations and 15 of gradient threshold, thresholding the images from 66 to 255 gray scale, ROI-shrink-wrap to obtain a region of interest (ROI) that contains all the sample, despeckle to remove black speckles with size lower than 64 voxels, and performing the 3D analysis.

Mechanical Analysis

Uniaxial compression and diametral testing were carried out on an Instron ElectroPuls E3000 testing machine (Instron, Norwood, USA), in ambient conditions, with gyroid-shaped disc designs. The loading rate was 0.5 mm/min until the occurrence of failure. A 5kN load cell was used. Compressive strength values (kgf/cm^2) were calculated by dividing the fracture load (F) by the cross-sectional area and converted into MPa. Diametral tensile strength values (kgf/cm^2) were calculated using the equation:

$$DTS = \frac{2F}{\pi dt}$$

where d is the specimen diameter, and t is the height of the specimen. DTS values were converted in MPa.

Three-point bending test was carried out on an Instron ElectroPuls E3000 testing machine (Instron, Norwood, USA), in ambient conditions. Rectangular bars were checked using a Digimatic caliper (Mitutoyo Absolute Digimatic Caliper, Tokyo, Japan). The bars were placed over two rods approximately 2.0 mm in diameter, with a 16.0-mm span length. A compressive force of 20 kgF load cell was applied in the center of the bars using a piston with 2.0 mm in diameter at a 0.5 mm/min crosshead speed to fracture. The flexural strength was measured as previously cited by Tavares *et al.*[41].

Blood compatibility test

To analyze the compatibility of the biomaterials with blood, the hemolysis assay was performed in duplicate as in previous studies[29,20]. First, 4 ml of anticoagulated sheep blood was diluted with 5 ml of normal saline 0.9%. For the positive and negative controls, 5 ml of Milli-Q water and 5 ml of normal saline 0.9% were used respectively. Biomaterials of the same size were submerged in tubes with 5 ml of normal saline. Then, 100 μl of diluted blood was added to each group and incubated at 37 °C for 60 min, followed by centrifugation at 1800 rpm for 10 min. Subsequently, the absorbance of the supernatant was taken at 540 nm in a spectrophotometer (Loccus LMR-96, Brazil). The hemolysis percentage was calculated as follows:

$$\%\ Hemolysis = \frac{A_S - A_{nc}}{A_{pc} - A_{nc}} \quad x\ \ 100\%$$

where A_s is the absorbance of the sample, A_{nc} is the absorbance of the negative control, and A_{pc} is the absorbance of the positive control.

Additionally, the results were confirmed with the hemolysis assay on blood agar, in which blood base media was prepared according to fabricant instructions (HIMEDIA, Ref. M158-500G). The agar base was cooled to 45 °C and mixed gently with sterile defibrinated sheep blood in a final concentration of 5% (vol/vol). Blood agar was poured into sterile Petri dishes and the scaffold samples were placed on solid agar and incubated at 37 °C for 24 and 48 hours.

Cell adhesion and viability

Scaffold samples were sterilized with 70% alcohol followed by UV light for 30 min at each site in a laminar flow. Then, the scaffolds were placed into 24 well plates, and MG63 cells (human osteosarcoma cell line) were seeded on the sample's upper surface at a cell density of 3500 cells/cm^2. Cells were cultured in Dulbecco's Modified Eagle's Medium (DMEM, Vitrocell, Ref D0025) supplemented with 10% fetal bovine serum (Vitrocell, Ref S0011), 1% penicillin/streptomycin (Vitrocell) and incubated at 37 °C with 5% $CO_{2.}$ For assessment of cell adhesion, the presence of attached cells on the samples was analyzed by SEM 24h after seeding. Then, the samples were washed with phosphate-buffered saline (PBS, pH 7.4), fixed in 10% formaldehyde for 30 min, rinsed in PBS, and dehydrated in ethanol series. The dried samples were metalized with a thin layer of gold. Images were acquired using TESCAN MIRA3 XMU equipment, see section 2.4.

Cell viability was examined with a resazurin-based assay (Sigma, Ref. 263-718-5) in triplicate and following the manufacturer's protocol on days 2, 5, and 7. Cells cultured directly on the 24-well cell culture plate (Kasvi, Ref. K12-024) were taken as the negative control.

Results and Discussion

Structural and chemical analysis

Figure 1(a) presents the XRD diffractograms for the three scaffolds, and it shows that all samples crystallized in the beta-phase of calcium phosphate without the presence of contaminants (β-TCP or β-$Ca_3(PO_4)_2$), independently of the temperature. This behavior is corroborated by a previous study by Jensen *et al* .[42]. Also, the scaffolds indicate a trigonal crystal system with a rhombohedral lattice, space group R3c, and international number 161. The atoms occupy the 6a and 18b Wyckoff positions, with different occupancy for some Ca, O, and P atoms. Figure 1(b) shows the crystalline structure of the material, with Ca^{2+} atoms in disordered octahedrons sharing an oxygen atom with PO_4^{3-} tetrahedral groups in the polyhedral corner. It is known that the partial occupancy and distortions of Ca^{2+} sites alter the occupancy and position of the phosphate groups, thus, altering the densification and properties of the material[43]. It is also known that β-TCP has five distinct Ca atoms, where the Ca(1), Ca(2), Ca(3), and Ca(5) are been discovered to be fully occupied with one Ca atom (occupancy factor of 1.0), meanwhile, the Ca(4) presents a three-fold coordination with oxygen atoms, leading to tetrahedral coordination, and it also presents a lower occupancy factor around 0.5[43]. Recently, Sblendorio *et al.* published a paper regarding the structural features of the β-TCP employing atomistic simulation, emphasizing the role of the Ca(4) atoms in the crystal structure. They presented that β-TCP could have seven different unit cell types, varying how many Ca(4) are occupied in the crystal structure[44]. This behavior showed that β-TCP can have a ratio of Ca/P ≠ 1.5, where values above 1.5 mean a higher occupancy of Ca(4) atomic sites, leading to an occupancy above 0.5. To obtain more information about the crystal structure, Rietveld refinement was performed in all the scaffolds. Figures 1(c,d,e) show the Rietveld refinement graphs

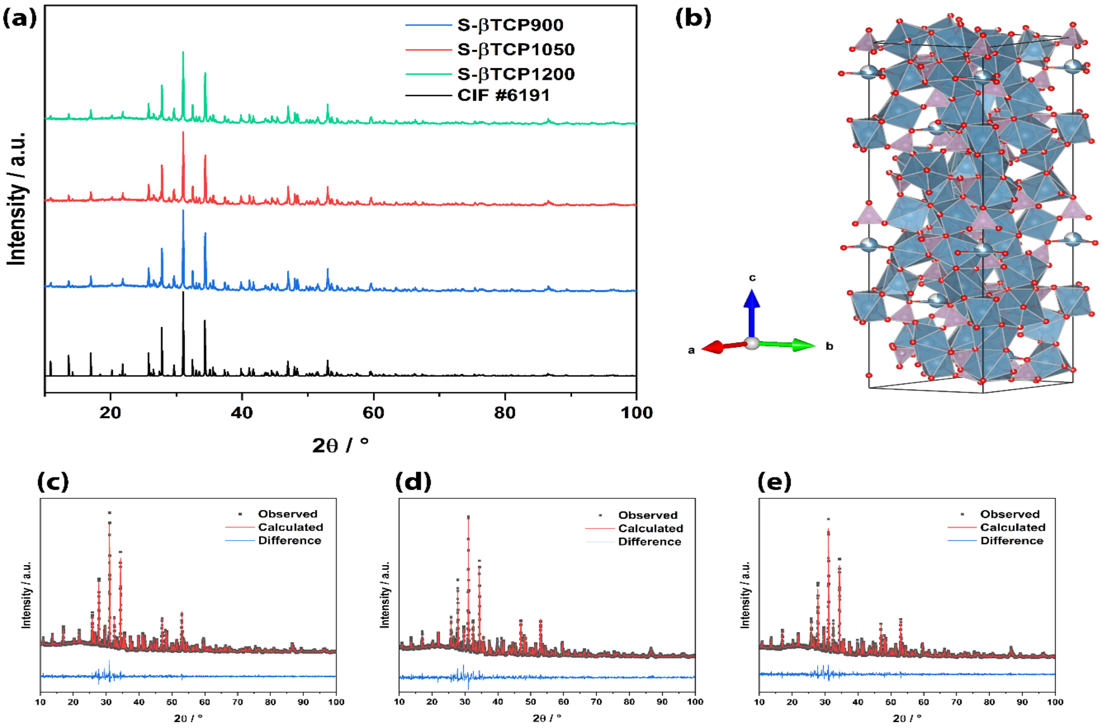

Figure 1 - (a) XRD data from scaffolds and the (b) crystal structure of the Calcium Phosphate - Rietveld refinement graphs of (c) S-βTCP900, (d) S-βTCP1050, and (e) S-βTCP1200 samples.

obtained for the S-βTCP900, S-βTCP1050, and S-βTCP1200 samples, respectively.

The difference curve between the experimental and calculated model shows good confidence in the Rietveld analysis since it appears almost flat for the samples in all the diffractogram regions. Table 1 shows quantitative data obtained through the refinement process, showing values for statistical R coefficients, where all samples presented $X^2 < 2.700$, indicating that the refinement process has chemical and physical meaning[45]. The Rietveld Refinement Data are presented in Supplementary Information. Interestingly, there are no major changes in the lattice parameters, however, it is noticeable significant changes in the Ca(4) occupancy as the sintering temperature increases.

The S-βTCP900 presented a lower Ca(4) occupancy of 0.5942, close to the standard CIF, which led to a Ca/P ratio of 1.513. Meanwhile, the S-βTCP1050 and S-βTCP1200 presented a sharp increase in the Ca(4) occupancy, leading to a higher Ca/P ratio of 1.531 and 1.542, respectively. Sblendorio *et al.* show that a Ca/P ratio higher than 1.500 means that there are more filled Ca(4) sites and the β-TCP has a supercell that is consistent with building blocks of several unit cells with different Ca(4) occupancy, leading to different crystalline structures that can affect its biochemical behavior[44]. Taking this information into account, the S-βTCP900 supercell may be composed of building blocks of three and four filled Ca(4) atomics sites, while the S-βTCP1050 and S-βTCP1200 can be composed of

Table 1 - Quantitative data from the Rietveld refinement of the samples and the standard CIF for comparison.

Sample	Lattice Parameters / Å	Ca(4) occupancy	Ca/P Ratio	Density / g.cm^{-3}	R_F / %	R_p / %	R_{wp} / %	X^2
S-βTCP900	a = b = 10.4231(7) c = 37.360(2)	0.5942	1.513	3.088	8.44	7.85	8.38	2.618
S-βTCP1050	a = b = 10.4196(1) c = 37.350(5)	0.7157	1.531	3.105	8.21	7.47	9.15	2.464
S-βTCP1200	a = b = 10.4233(5) c = 37.36(3)	0.7954	1.542	3.120	8.15	6.61	8.39	2.010
Standard CIF - ICSD #6191	a = b = 10.439(0) c = 37.37(5)	0.4910	1.5000	3.140				

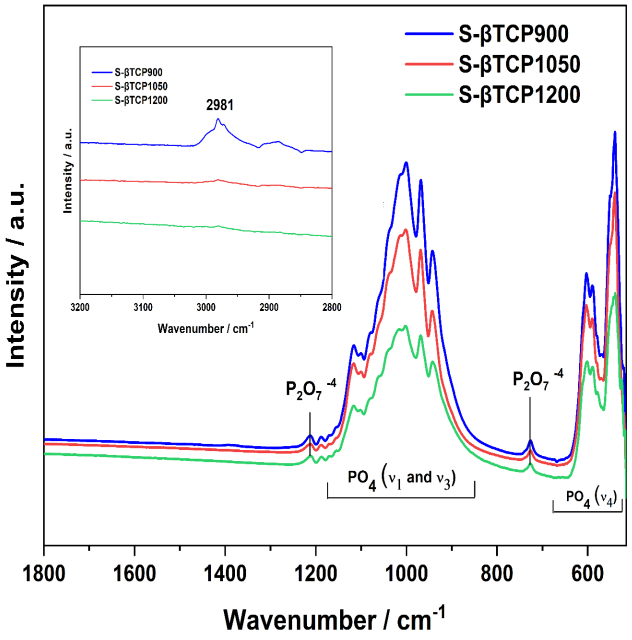

Figure 2 - FTIR spectra of the β-TCP scaffolds.

building blocks of four or five filled Ca(4) sites. These behaviors are closely related to the density of the material and its final structure. It is worth mentioning that this behavior is still undergoing investigation in the literature, and the characteristics of the Ca(4) site cannot be accounted for by employing only one unit cell, but a combination of the seven types found in Sblendorio's work, which could lead to errors in the analysis.

Figure 2 shows the functional groups present in the scaffolds, identified using Fourier-transform infrared (FTIR) spectroscopy. The spectra of the samples exhibited similarities in the functional groups. The v_3 vibrational mode of the PO_4^{3-} ion was attributed to stretching peaks observed at 1008, 1015, 1080, 1100, and 1115 cm^{-1}. The v_1-PO_4 mode was observed at 945 and 970 cm^{-1}, while the v_4-PO_4 mode was observed at 605, 592, 552, and 540 cm^{-1}. Changes in the intensity of the stretching peaks were noted with variations in the sintering temperature, consistent with previous findings[46]. Furthermore, less intense peaks were observed at 726 and 1212 cm^{-1}, characteristic of the pyrophosphate group ($P_2O_7^{-4}$ species). This observation may be attributed to a non-stoichiometric balance between Ca/P ions in the crystalline structure, which can be related to the Ca(4) atomic site[47], consistent with the results obtained from XRD and Rietveld refinement analyses. It is worth mentioning that there is no observation of carbonyl peaks around 1680 cm^{-1}. However, the inset inside Figure 2 presents small intensity vibrations around 2981, 2950, and 2910 cm^{-1} for the S-βTCP900, attributed to the stearic acid of the initial ink. This shows that the initial ink was fully removed during the sintering process of the S-βTCP1050 and S-βTCP1200 samples[48].

Figure 3 shows the SEM images obtained for the scaffolds. It is clear the changes in the morphology and texture of the 3D-printed scaffolds when the sintering temperature increases, with a smoothing process of the particles on the top of the scaffold filament. It is noticeable that the scaffold filament size shrinks with the thermal treatment, going to 322 ± 14, 275 ± 13, and 251 ± 15 μm for the S-βTCP900, S-βTCP1050, and S-βTCP1200 samples, respectively. This information is also presented in Table 2, for comparison purposes of the measured filament size between SEM and μCT analysis. This behavior occurs due to the sintering process and the coalescence between particles, which can be seen in Figures 3(b,e,h), where the S-βTCP900 sample presents detached particles on the surface with a granular morphology, creating a loosely porous network that occurs between

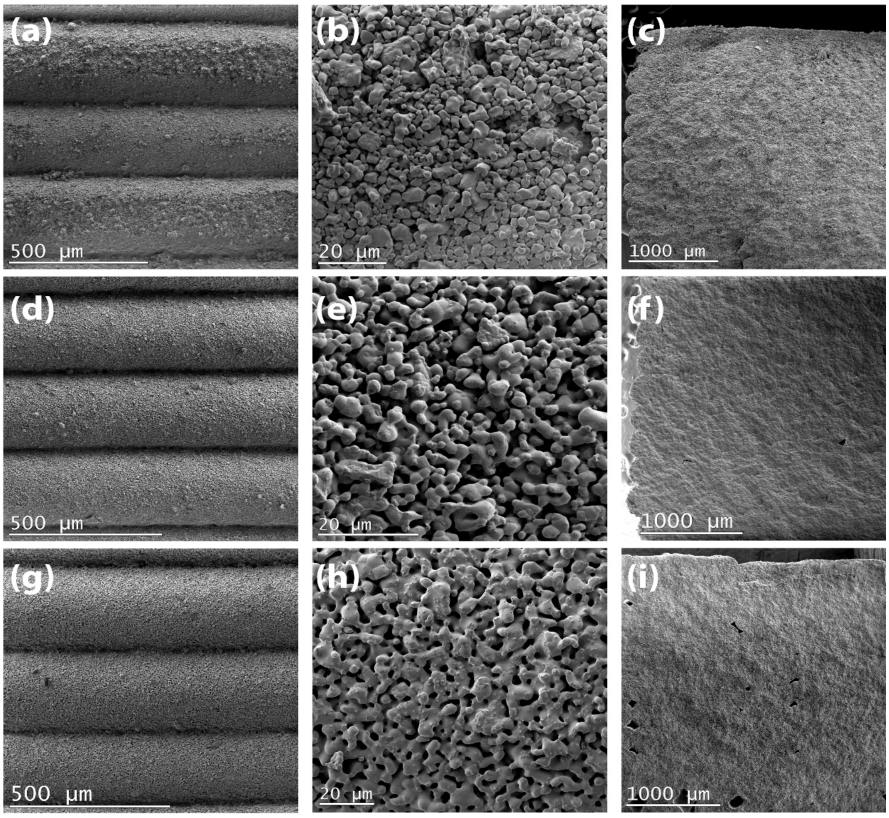

Figure 3 - SEM images of the (a,b,c) S-βTCP900, (d,e,f) S-βTCP1050, and (g,h,i) S-βTCP1200 samples showing the filament top view, filament top view at higher magnification, and side fracture of the scaffolds, respectively.

particles, which do not have strong interaction and coalescence. Meanwhile, the S-βTCP1050 sample presents fewer detached particles and the beginning of coalescence between particles, showing a more efficient sintering process with less granular regions, which directly impacts the mechanical properties, pore size distribution, surface morphology, and cell adhesion and viability properties[49]. Finally, the S-βTCP1200 sample shows a complete coalescence between particles and an optimal sintering process, where the particles are completely connected and it creates a small porous network, with some pores ranging between 1 and 30 µm. However, Figures 3(c, f, i) shows the side view of the scaffold fracture, presenting an interesting behavior. The sintering temperature increase caused the formation of big pores around 100 – 300 µm inside the structure, correlated with the coalescence between particles, that start to bind together, creating empty spaces in the 3D printed structure. This behavior is very important for biomaterial, where a previous study shows the importance of a range of pore sizes to improve cell growth on 3D printed scaffolds, where small pores (1 – 30 µm) are important for mass and nutrient transfer, and bigger pores are good for cell attachment[50].

To study the sintering process using the µCT technique, it is necessary to follow a strict method of reconstruction due to the lack of information about this methodology in the literature[51]. A work by Cengiz *et al.* shows the importance of giving the most information possible to reproduce µCT analysis, and that there is a small number of papers reporting the mineral density of ceramic materials[52]. However, past works presented a way to obtain information about the mean values of greyscale pixels for the volumetric reconstruction, showing the possibilities of obtaining information about the densification of biomaterials[53]. In this sense, we used the same histogram start and end points of the 16-bit TIFF grayscale images to select the same pixels for all scaffolds during the NRecon reconstruction, ranging the attenuation coefficient from 0.013647 to 0.034850, and the same parameters for smoothing (value = 3), beam-hardening correction (10%), a rectangular region of interest (ROI), and image rotation when needed. This gave us the confidence to analyze the materials in the same pixel density and range, between 0 to 65434 gray levels (0 the pure black and 65434 pure white color), thus providing confidence in analyzing and comparing the materials in this study. We filtered the transfer function in the opacity channel to show only the pixels with grayscale values between 45200 – 65434, and applied it to all analyses, providing information about the dense regions in the scaffolds.

Figure 4 presents the volumetric reconstruction of the scaffolds, showing the whole sample (Figures 4(a,d,g)) with no transfer function editing, and the transversal and longitudinal view of the samples with the applied transfer function mentioned before. The S-βTCP1200 and S-βTCP1050 possess more dense regions than S-βTCP900, which is correlated to the sintering process of the materials. The S-βTCP900 presents dense regions around the edges of the piece, showing that the sintering process was not that efficient, and the dense regions respect the usual heat flow during the sintering process, coming out of the edges into the core of the sample, and it is clear in Figures 4(b,c) that in the center of the sample, there are no dense particles. Meanwhile, the samples S-βTCP1050 and S-βTCP1200 present more dense particles, thus showing that the sintering process is more efficient at temperatures higher than 1050 °C, corroborating SEM images.

Table 2 presents the results of the quantitative analysis conducted using µCT. It was observed that the filament size decreased with increasing sintering temperature, indicating a tendency for contraction of the β-TCP ceramic. The porosity is also affected by the sintering process, showing a decrease in the total porosity. The S-βTCP900 shows the highest porosity values, with a small value of mean pore size. The closure of some of those pores occurs for the S-βTCP1050 and S-βTCP1200 samples, leading to a sharp increase in the mean pore size.

To further assess the behavior of pore size increase, Figure 5 illustrates the pore size distribution derived from quantitative analysis using micro-CT data. The S-βTCP900 sample exhibits over 50% of its pores within the range of 6 to 30 µm. This range corresponds to the gaps observed between granular particles on the material's surface, as depicted in Figure 3(b, e, h). It is noteworthy that the frequency of smaller pore sizes decreases with the rise in sintering temperature. Specifically, the percentage of pores ranging from 6 to 30 µm decreases to approximately 13% for S-βTCP1050 and 8% for S-βTCP1200. The emergence of larger pores contributes to a more uniform distribution of pore sizes. Figures 5(b, c) illustrate a higher frequency of pores with sizes exceeding 100 µm. Interestingly, S-βTCP1200 is the sole sample surpassing the small porosity region, featuring two distinct regions with a Gaussian behavior labeled as Region 1 (red) and Region 2 (green). These regions significantly contribute to the mean pore size compared to the region of pores < 30 µm. This behavior is associated with the formation of larger pores observed in Figures 3(c, f, i). The formation of larger pores can be attributed to the removal of stearic acid, as shown in Figure 2, during the S-βTCP1050 and S-βTCP1200 sintering processes. This removal process may act as a porogen agent[54,55], creating a macroporous structure and different porous regions, which can be beneficial for cell adhesion and proliferation[31]. Recently, a work by Ossiform® also showed a microstructural evaluation of 3D-printed β-TCP scaffolds, corroborating the results presented in our work, such as small pores generated by the sintering process and variations depending on the thermal treatment of the samples[56].

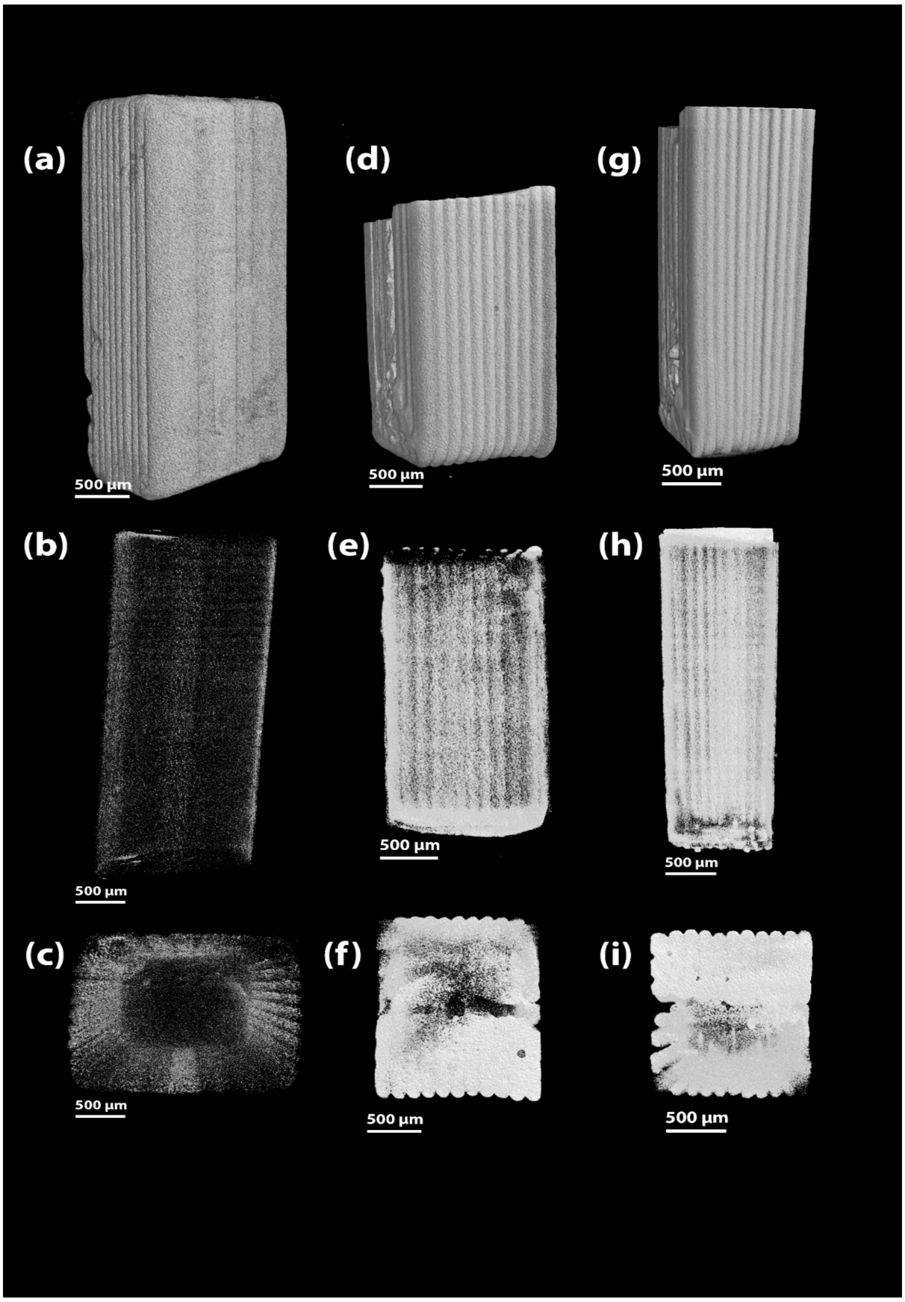

Figure 4 - X-ray µCT reconstructed images showing the whole piece for (a) S-βTCP900, (d) S-βTCP1050, and (g) S-βTCP1200 samples. Images of the transversal and longitudinal directions, respectively, of the transfer function-filtered scaffolds for the (b,c) S-βTCP900, (e,f) S-β-TCP1050, and (h, i) S-βTCP1200.

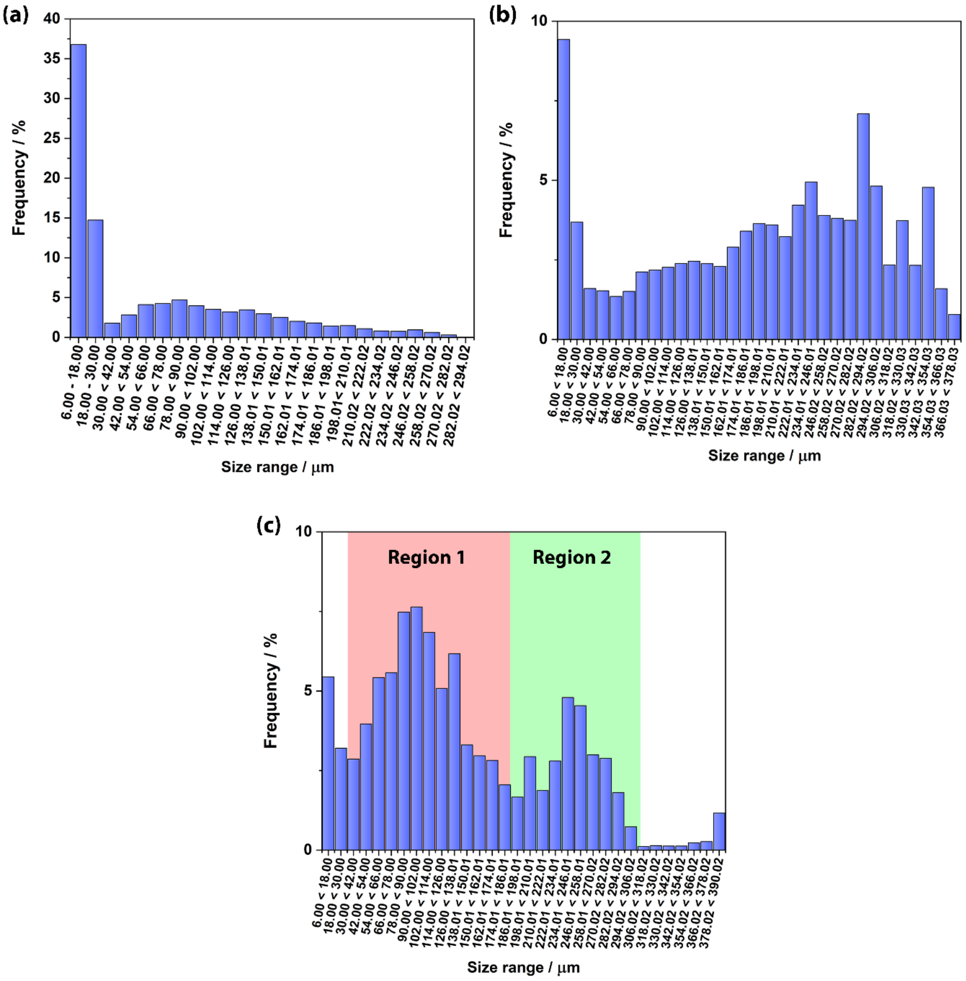

Figure 5 - Pore size distribution of the (a) S-βTCP900, (b) S-βTCP1050, and (c) S-βTCP1200. The quantitative data was obtained through microCT analysis.

Mechanical Analysis

The S-βTCP1200 presented the highest flexural strength values (22.2 ± 4.2 MPa) when evaluated in the three-point bending test, followed by the S-βTCP1050 (10.8 ± 0.6) and then the S-βTCP900 (1.6 ± 1.9) ($p<0.001$), Figure 6. Regarding the axial compressive test, the same behavior was observed. The S-βTCP1200 (46.0 ± 4.8 MPa) showed higher strength when compared to S-βTCP1050 (13.8 ± 1.7) and S-βTCP900 (2.9 ± 1.0) ($p<0.001$). These results can be influenced by micropores contained in scaffolds, with a total porosity varying from ~17% (for S-βTCP900) to ~3% (for S-βTCP1200) (Table 2).

The values are comparable with those achieved with 3D printed TCP sintered at 1100 °C (11.6 ± 2.1 MPa). However, it is important to highlight that because of an increase of 100 °C in sintering temperature, we found the average strength of the sintered samples to be 46 MPa (S-βTCP1200), this was significantly higher than the 11 MPa found in a previously published report for the same material[57].

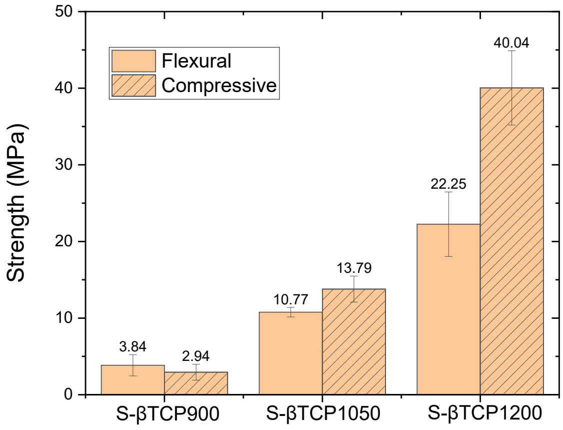

Figure 6 - (a) Flexural strength and (b) axial compressive for S-βTCP900, S-βTCP1050, and S-βTCP1200. Graphs show average values ± standard deviation.

Table 2 - Porosity parameters and filament thickness measurements obtained by μCT analysis for β-TCP scaffolds sintered at different temperatures.

Sample	*Filament thickness[1] / μm*	*Filament thickness[2] / μm*	*Open Porosity / %*	*Closed Porosity / %*	*Total Porosity / %*	*Mean Pore size / μm*
S-βTCP900	300 ± 23	322 ± 14	14.64	2.31	16.95	17 ± 7
S-βTCP1050	269 ± 17	275 ± 13	3.66	0.53	4.19	196 ± 107
S-βTCP1200	225 ± 23	251 ± 15	2.44	0.39	2.83	139 ± 86

Blood compatibility tests

The hemolysis test is based on the degree of erythrocyte lysis when the biomaterial comes into contact with these cells *in vitro*. Then, a lower hemolysis percentage suggests good blood compatibility. Figure 7a illustrates the hemolysis percentage of the biomaterials. As expected, the biomaterials had a hemolysis percentage similar to the negative control, suggesting that these were highly hemocompatible (Figure 7b). Also, no hemolysis halo was detected on blood agar after 24 and 48 hours (see Figure 7 c-d), confirming the previous results. Then, the sintering temperature of 3D biomanufactured **β**-TCP scaffolds did not interfere with the scaffolds' blood compatibility.

Cell adhesion and viability

The SEM analysis was performed 24h after cell seeding to verify adhesion on the scaffolds and employing the backscattered electron (BSE) detector, where regions with higher atomic numbers (such as calcium and phosphorous) will appear brighter, while a lower atomic number appears darker in the image (such as cell-matrix). Figure 8(a-f) shows that cells were able to adhere to the scaffold's surface. Also, a higher cell density was seen on the S-**β**TCP1200 (Figure 8f), suggesting an excellent interaction between cells and scaffolds. Moreover, MG63 cells presented a typical morphology with elongated cell processes in the S-**β**TCP1200, while S-**β**TCP900 and S-**β**TCP1050

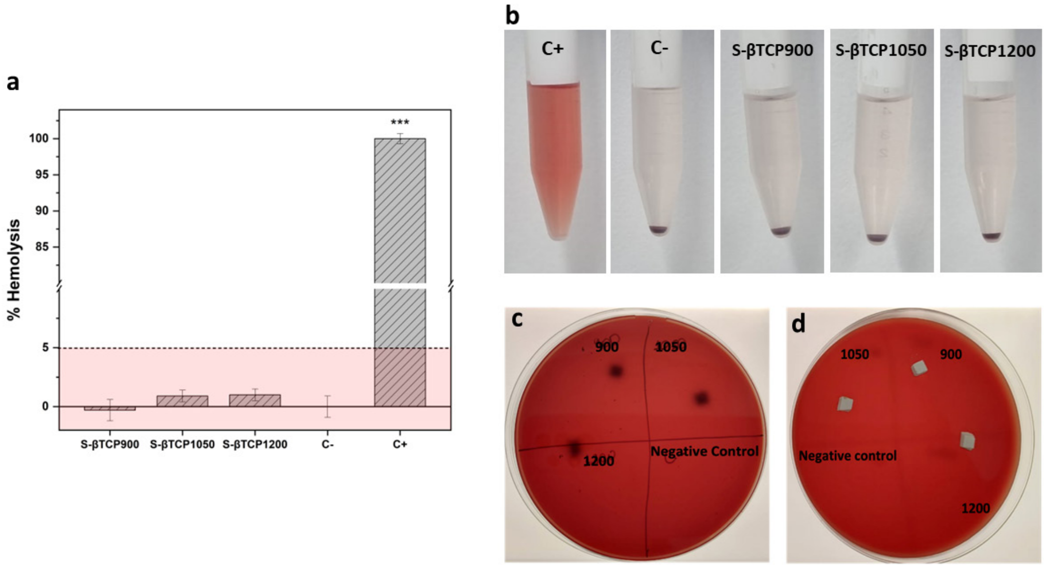

Figure 7 - Blood compatibility test. (a) Hemolysis percentage of scaffolds. (b) Illustration of hemolysis assay. (c) Hemolysis on blood agar after 24h, back of the Petry dish. (d) Hemolysis on blood agar after 48h, front of the Petry dish.

exhibited rounded morphology. Mealy *et al*. found that sintering temperatures are associated with surface topography, described as wavelength (**λ**), thereby higher sintering temperatures providing a larger basal contact area with more adhesion sites for cells[58]. Conversely, they suggested that the granular surface topography obtained at low sintering temperatures provides insufficient contact area for cell attachment. Similarly, Dulgar *et al*.[57] suggested that ceramics with higher grain sizes obtained at higher sintering temperatures led to enhanced cell adhesion and proliferation. Then, in our study, the coalescence between particles in S-**β**TCP1200 could explain better cell adhesion due to the presence of a larger basal contact area for cells.

Regarding cell viability, Figure 9 shows no difference between the S-**β**TCP1200 group and the negative control at each time. However, a significant difference between the both groups and, S-**β**TCP900 and S-**β**TCP1050 was seen on days 5 and 7. These results could be explained due to reduced cell adhesion observed on S-**β**TCP900 since cell adhesion is crucial for subsequent cell functions such as proliferation, and protein synthesis. Additionally, the improved mechanical properties with higher scaffold density and strength in the S-**β**TCP1200 may contribute to these differences. Previous studies showed that higher mechanical properties enhance osteoblastic function[52,53]. This enhancement could be attributed to the cells' ability to sense their extracellular

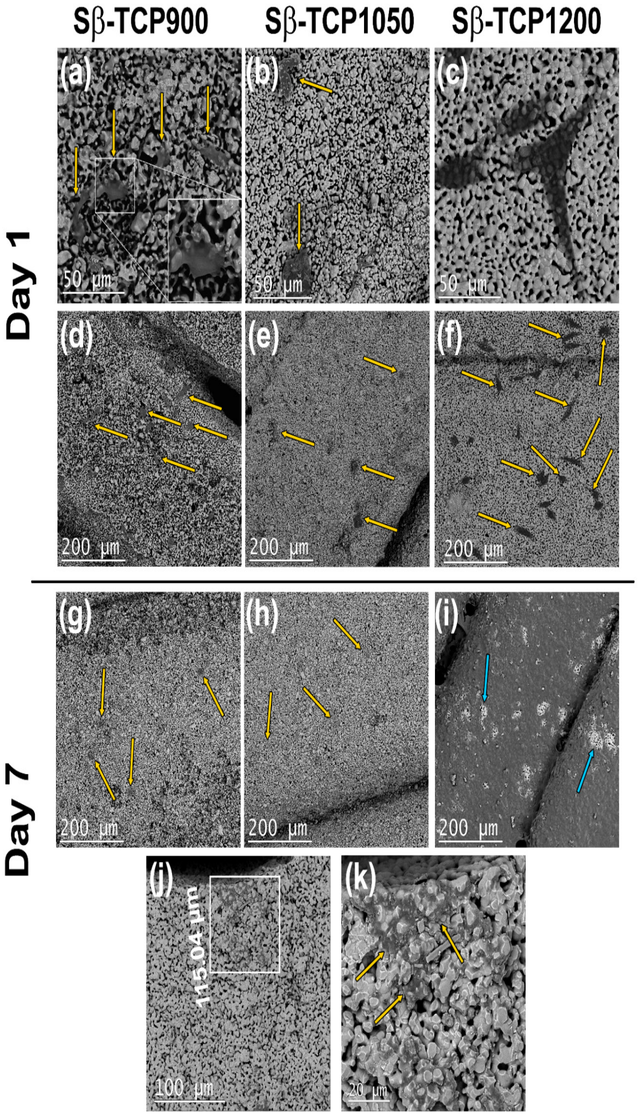

Figure 8 - Backscattered Electron - SEM images of the top view of scaffolds (S-βTCP900, S-βTCP1050 and S-βTCP1200) cultivated with cells at (a-f) day 1 and (g-i) day 7. The (j) cross-section cut of the S-βTCP1200 and (k) a higher magnification of the squared region of (j). Yellow arrows indicate the cells and blue arrows indicate details of the material without cells.

environment mechanosensitive and modulate cell attachment, proliferation, and differentiation based on substrate stiffness[61,62]. This implies that cells can respond to the mechanical properties of the scaffolds by rearranging cytoskeletal elements and activating mechanotransduction signaling pathways[63]. Figure 8(g-i) shows SEM images of the scaffolds on day 7, where is possible to see a layer of MG63 cells (dark gray) coating the surface of the scaffold in S-**β**TCP1200 (Figure 8i), and the blue arrows indicate the areas without cells in light grey. In the rest of the scaffolds, the formation of cell layers was not evident on day 7. Moreover, S-**β**TCP1200 presented some areas of cell infiltration into the scaffold (around 115 μm) as is shown in Figure 8 (j-k), probably due to the higher pore size of the scaffold facilitating cell migration. Future studies will explore the impact of different scaffold geometries on the structural and biological properties of 3D-printed β-TCP scaffolds. Additionally, microCT imaging will be employed to analyze in vivo assays, providing detailed insights into scaffold integration and performance in bone regeneration.

Conclusion

In summary, this study evaluated the influence of the sintering process on the microstructure, cell, and blood compatibility of 3D-printed **β**-TCP scaffolds. Sintering temperatures above 1050 °C showed higher densification with improved mechanical properties, with no detached particles on the surface. Interestingly, during the sintering process of the scaffolds, bigger pores emerged inside the structure, and the filament had a size shrinkage due to the coalescence between particles, but kept its final structure intact. These characteristics produced scaffolds with enhanced mechanical properties and allowed MG63 osteoblast-like cells to penetrate the scaffold and proliferate on the top of the scaffold and inter filaments. These findings show that tailoring the sintering process of 3D-printed **β**-TCP scaffolds can modulate its structural properties maintaining good cell viability, making the materials a good choice for clinical trials analyzing its performance in regenerating different bone regions.

Acknowledgments

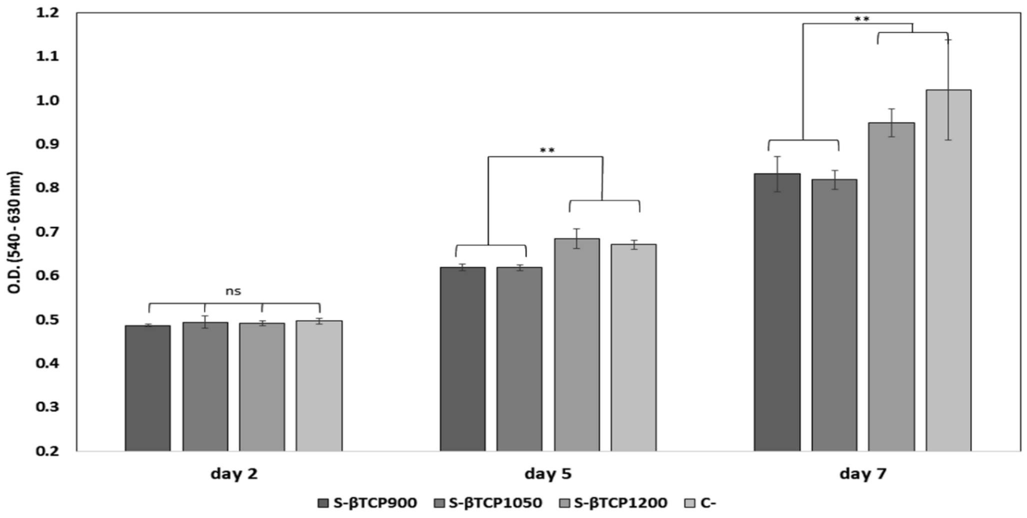

Figure 9 - Cell viability after 2, 5, and 7 days of culture in the scaffolds. Data expressed as the mean ± SD. *P ≤ 0.05 and **P ≤ 0.01 indicates significance between groups and "ns" no significance by one-way ANOVA followed by Tukey HSD post hoc test (n=3). Negative control: cell culture plate. O.D.: Optical density.

First, we honor and express our heartfelt gratitude in memory of Jorge Vicente Lopes da Silva for his unwavering dedication to science and society. As a founding member of the 3D technology and Biofabrication Group at the CTI Renato Archer, he made a significant impact on Brazilian science and society as a researcher and humanitarian person. His passion and commitment to advancing knowledge will continue to inspire generations to come. Thank you.

This work was supported by the National Council for Scientific and Technological Development (CNPq - 312216/2017-3, 444303/2018-9 and 407680/2021-7), and the Coordination for Improvement of Higher Education Personnel - Brazil (CAPES) - Funding Code 001. K. N. Ferreira thanks FAPESP for the financial support (2024/06681-4). L.E. Carneiro-Campos thanks Ossiform® (Denmark), for the collaboration for the development of new technologies for bone tissue repair, and Prof. C. J. Soares, P. D. Barbar, and the postgraduate program in dentistry at the Federal University of Uberlandia (Brazil) for the support received by the biomechanical analysis laboratory. We would like to thank FINEP for the financial support of the EMITUSAÚDE (01.18.0027.01) project on the acquisition of the X-ray microtomography equipment. J. Daguano thanks COLAB, open facilities of CTI Renato Archer.

References

[1]. Hu J, Zhou Y, Huang L, Liu J, Lu H. Effect of nano-hydroxyapatite coating on the osteoinductivity of porous biphasic calcium phosphate ceramics. BMC Musculoskelet Disord. 2014 Apr 1;15:114. https://link.springer.com/article/10.1186/1471-2474-15-114

[2]. Fardin AC, Jardim ECG, Pereira FC, Guskuma MH, Aranega AM, Garcia Júnior IR. Bone graft in dentistry: review of literature. Innovations Implant Journal. 2010 Dec;5(3):48–52. http://revodonto.bvsalud.org/scielo.php?pid=S1984-59602010000300010&script=sci_arttext&tlng=en

[3]. Giannoudis PV, Dinopoulos H, Tsiridis E. Bone substitutes: an update. Injury. 2005 Nov;36 Suppl 3. https://doi.org/10.1016/j.injury.2005.07.029

[4]. Horta R, Frias F, Jarnalo M, Teixeira S, Silva P, Oliveira I, Silva A. Facial Reconstruction Based on Combined Three-Dimensional Printing and Microsurgical Free Transfer. The Journal of Craniofacial Surgery. 2020 June;31(4). https://doi.org/10.1097/scs.0000000000006559

[5]. Chang B, Liu X. Osteon: structure, turnover, and regeneration. Tissue Eng., Part B. 2022;28(2):261–278. https://doi.org/10.1089/ten.teb.2020.0322

[6]. Qin Q, Lee S, Patel N, et al. Neurovascular coupling in bone regeneration. Exp. Mol. Med. 2022;54(11):1844–1849. https://www.nature.com/articles/s12276-022-00899-6

[7]. Sparks DS, Savi FM, Dlaska CE, et al. Convergence of scaffold-guided bone regeneration principles and microvascular tissue transfer surgery. Sci. Adv. 2023;9(18). https://pubmed.ncbi.nlm.nih.gov/37146134/

[8]. Megías R, Vercher-Martínez A, Belda R, et al. Numerical modelling of cancellous bone damage using an orthotropic failure criterion and tissue elastic properties as a function of the mineral content and microporosity. Comput. Methods Progr. Biomed. 2022;219:106764. https://doi.org/10.1016/j.cmpb.2022.106764

[9]. Langdahl B, Ferrari S, Dempster DW. Bone modeling and remodeling: potential as therapeutic targets for the treatment of osteoporosis. Ther. Adv. Musculoskelet. Dis. 2016;8(6):225–235. https://pubmed.ncbi.nlm.nih.gov/28255336/

[10]. Dixit K, Gupta P, Kamle S, et al. Structural analysis of porous bioactive glass scaffolds using micro-computed tomographic images. J Mater Sci. 2020;55:12705–12724. https://doi.org/10.1007/s10853-020-04850-w

[11]. Rajagopalan S, Lu L, Yaszemski MJ, et al. Optimal segmentation of microcomputed tomographic images of porous tissue-engineering scaffolds. J Biomed Mater Res A. 2005;75A:877–887. https://doi.org/10.1002/jbm.a.30498

[12]. Bohner M, Santoni BLG, Döbelin N. β-tricalcium phosphate for bone substitution: Synthesis and properties. Acta Biomater. 2020;113:23–41. https://doi.org/10.1016/j.actbio.2020.06.022

[13]. Causa F, Netti PA, Ambrosio L, et al. Poly-e-caprolactone/hydroxyapatite composites for bone regeneration: in vitro characterization and human osteoblast response. J Biomed Mater Res. 2006;76:151e62. https://doi.org/10.1002/jbm.a.30528

[14]. Chuenjitkuntaworn B, Inrung W, Damrongsri D, et al. Polycaprolactone/hydroxyapatite composite scaffolds: preparation, characterization, and in vitro and in vivo biological responses of human primary bone cells. J Biomed Mater Res. 2010;94:241e51. https://doi.org/10.1002/jbm.a.32657

[15]. Decante G, Costa JB, Silva-Correia J, et al. Engineering bioinks for 3D bioprinting. Biofabrication. 2021;13:032001. https://doi.org/10.1088/1758-5090/abec2c

[16]. Chavez T, Gerecht S. Engineering of the microenvironment to accelerate vascular regeneration. Trends Mol. Med. 2023;29(1):35–47. https://doi.org/10.1016/j.molmed.2022.10.005

[17]. Ma Y, Lin M, Huang G, et al. 3D spatiotemporal mechanical microenvironment: a hydrogel-based platform for guiding stem cell fate. Adv. Mater. 2018;30(49) https://doi.org/10.1002/adma.201705911

[18].Sherwood JK, Riley SL, Palazzolo R, et al. A three-dimensional osteochondral composite scaffold for articular cartilage repair. Biomaterials. 2002;23:4739e51. https://doi.org/10.1016/s0142-9612(02)00223-5

[19].Hutmacher DW, Schantz T, Zein I, et al. Mechanical properties and cell cultural response of polycaprolactone scaffolds designed and fabricated via fused deposition modeling. J Biomed Mater Res. 2001;55:203e16. https://doi.org/10.1002/1097-4636(200105)55:2%3C203::AID-JBM1007%3E3.0.CO;2-7

[20].Sadtler K, Wolf MT, Ganguly S, et al. Divergent immune responses to synthetic and biological scaffolds. Biomaterials. 2019;192:405e15. https://doi.org/10.1016/j.biomaterials.2018.11.002

[21].Zhang S, Hu B, Liu W, et al. Articular cartilage regeneration: the role of endogenous mesenchymal stem/ progenitor cell; recruitment and migration. Semin Arthritis Rheum. 2020;50:198e208. https://doi.org/10.1016/j.semarthrit.2019.11.001

[22].Im G-I. Endogenous cartilage repair by recruitment of stem cells. Tissue Eng Part B. 2016;22:160e71. https://doi.org/10.1089/ten.teb.2015.0438

[23].Bigi A, Boanini E. Functionalized biomimetic calcium phosphates for bone tissue repair. J Appl Biomater Funct Mater. 2017 Nov 10;15(4). https://doi.org/10.5301/jabfm.5000367

[24].Posner AS, Beebe RA. The surface chemistry of bone mineral and related calcium phosphates. Semin Arthritis Rheum. 1975 Feb;4(3):267–91. https://doi.org/10.1016/0049-0172(75)90013-X

[25].Jensen MB, Slots C, Ditzel N, et al. Treating mouse skull defects with 3D-printed fatty acid and tricalcium phosphate implants. J Tissue Eng Regen Med. 2020 Dec;14(12):1858–68. https://doi.org/10.1002/term.3146

[26].Boyce BF, Xing L. Biology of RANK, RANKL, and osteoprotegerin. Arthritis Res Ther. 2007;9 Suppl 1. https://doi.org/10.1186/ar2165

[27].Vanden Berg-Foels WS. In situ tissue regeneration: chemoattractants for endogenous stem cell recruitment. Tissue Eng Part B. 2014;20:28e39. https://www.liebertpub.com/doi/abs/10.1089/ten.teb.2013.0100

[28].Indurkar A, Choudhary R, Rubenis K, et al. Advances in sintering techniques for calcium phosphates ceramics. Mater. 2021;14(10). https://doi.org/10.3390/ma14206133

[29].Umemoto S, Furusawa T, Unuma H, et al. In vivo bioresorbability and bone formation ability of sintered highly pure calcium carbonate granules. Dent Mater J. 2021;40:1202–1207. https://doi.org/10.4012/dmj.2020-254

[30].Bolander J, Chai YC, Geris L, et al. Early BMP, Wnt and Ca 2þ /PKC pathway activation predicts the bone forming capacity of periosteal cells in combination with calcium phosphates. Biomater. 2016;86:106-118. https://doi.org/10.1016/j.biomaterials.2016.01.059.

[31].Slots C, Jensen MB, Ditzel N, et al. Simple additive manufacturing of an osteoconductive ceramic using suspension melt extrusion. Dent Mater. 2017;33:198–208. https://doi.org/10.1016/j.dental.2016.11.012

[32].Montelongo SA, Chiou G, et al. Development of bioinks for 3D printing microporous, sintered calcium phosphate scaffolds. J Mater Sci Mater Med. 2021;32:94 3-16. DOI: 10.1007/s10856-021-06569-9. https://doi.org/10.1007/s10856-021-06569-9

[33].Bouakaz, I., Drouet, C., Grossin, D., Cobraiville, E., & Nolens, G. (2023). Hydroxyapatite 3D-printed scaffolds with Gyroid-Triply periodic minimal surface porous structure: Fabrication and an in vivo pilot study in sheep. Acta Biomaterialia, 170, 580–595. https://doi.org/10.1016/j.actbio.2023.08.041

[34]. Budharaju, H., Suresh, S., Sekar, M. P., de Vega, B., Sethuraman, S., Sundaramurthi, D., & Kalaskar, D. M. (2023). Ceramic materials for 3D printing of biomimetic bone scaffolds – Current state-of-the-art & future perspectives. Materials & Design, 231, 112064. https://doi.org/10.1016/J.MATDES.2023.112064

[35].Thygesen, T., Slots, C., Jensen, M. B., Ditzel, N., Kassem, M., Langhorn, L., & Andersen, M. (2022). Comparison of off-the-shelf β-tricalcium phosphate implants with novel resorbable 3D printed implants in mandible ramus of pigs. Bone, 159, 116370. https://doi.org/10.1016/J.BONE.2022.116370

[36].Zhao, X., Li, N., Zhang, Z., Hong, J., Zhang, X., Hao, Y., Wang, J., Xie, Q., Zhang, Y., Li, H., Liu, M., Zhang, P., Ren, X., & Wang, X. (2024). Beyond hype: unveiling the Real challenges in clinical translation of 3D printed bone scaffolds and the fresh prospects of bioprinted organoids. Journal of Nanobiotechnology, 22(1). https://doi.org/10.1186/S12951-024-02759-Z

[37].Podgórski, R., Wojasiński, M., Małolepszy, A., Jaroszewicz, J., & Ciach, T. (2024). Fabrication of 3D-Printed Scaffolds with Multiscale Porosity. ACS Omega, 9(27), 29186–29204. https://doi.org/10.1021/ACSOMEGA.3C09035/ASSET/IMAGES/LARGE/AO3C09035_0012.JPEG

[38].Slavin, B. v., Mirsky, N. A., Stauber, Z. M., Nayak, V. V., Smay, J. E., Rivera, C. F., Mijares, D. Q., Coelho, P. G., Cronstein, B. N., Tovar, N., & Witek, L. (2024). 3D printed β-tricalcium phosphate versus synthetic bone mineral scaffolds: A comparative in vitro study of biocompatibility. Bio-Medical Materials and Engineering, 35(4), 365–375. https://doi.org/10.3233/BME-230214

[39].Toby BH. EXPGUI, a graphical user interface for GSAS. J Appl Crystallogr 2001; 34: 210–213. DOI: 10.1107/S0021889801002242

[40].Momma K, Izumi F. VESTA 3 for three-dimensional visualization of crystal, volumetric and morphology data. J Appl Crystallogr 2011; 44: 1272–1276.). https://doi.org/10.1107/S0021889811038970

[41].Tavares LN, Zancopé K, Silva ACA, et al. Microstructural and mechanical analysis of two CAD-CAM lithium disilicate glass-reinforced ceramics. Braz Oral Res 2020; 31:34 e004. https://doi.org/10.1590/1807-3107bor-2020.vol34.0004

[42].Wang L, Nancollas GH. Calcium orthophosphates: Crystallization and Dissolution. Chem Rev 2008; 108: 4628–4669. https://doi.org/10.1021/cr0782574

[43].Yashima M, Sakai A, Kamiyama T, et al. Crystal structure analysis of β-tricalcium phosphate Ca3(PO4)2 by neutron powder diffraction. J Solid State Chem 2003; 175: 272–277. https://doi.org/10.1016/S0022-4596(03)00279-2

[44].Sblendorio GA, Le Gars Santoni B, Alexander DTL, et al. Towards an improved understanding of the β-TCP crystal structure by means of "checkerboard" atomistic simulations. J Eur Ceram Soc 2023; 43: 3746–3754. https://doi.org/10.1016/j.jeurceramsoc.2023.02.036

[45].Toby BH. R factors in Rietveld analysis: How good is good enough? Powder Diffr 2006; 21: 67–70. https://doi.org/10.1154/1.2179804

[46].Gibson IR, Rehman I, Best SM, et al. Characterization of the transformation from calcium-deficient apatite to β-tricalcium phosphate. J Mater Sci Mater Med 2000; 11: 799–804. https://doi.org/10.1023/A:1008905613182

[47].Theophanides T, Theophanides T. Introduction to Infrared Spectroscopy. Infrared Spectroscopy - Materials Science, Engineering and Technology. Epub ahead of print 25 April 2012. DOI: 10.5772/49106.

[48].Mao C, Lu J, Xu Q, et al. FTIR study of hydrogen bonding of stearic acid with ethanol, dimethyl sulfoxide, and acetonitrile in supercritical CO2. Chin J Chem 1999; 17: 223–230. https://doi.org/10.1002/cjoc.19990170304

[49].Cun X, Hosta-Rigau L. Topography: A Biophysical Approach to Direct the Fate of Mesenchymal Stem Cells in Tissue Engineering Applications. Nanomater 2020; 10(10): 2070. https://doi.org/10.3390/nano10102070

[50].Han Y, Lian M, Wu Q, et al. Effect of Pore Size on Cell Behavior Using Melt Electrowritten Scaffolds. Front Bioeng Biotechnol 2021; 9: 629270. https://doi.org/10.3389/fbioe.2021.629270

[51].Ho ST, Hutmacher DW. A comparison of micro CT with other techniques used in the characterization of scaffolds. Biomater 2006; 27: 1362–1376. https://doi.org/10.1016/j.biomaterials.2005.08.035

[52].Cengiz IF, Oliveira JM, Reis RL. Micro-CT – a digital 3D microstructural voyage into scaffolds: a systematic review of the reported methods and results. Biomater Res 2018; 22: 1–11. https://doi.org/10.1186/s40824-018-0136-8

[53].Keklikoglou K, Arvanitidis C, Chatzigeorgiou G, et al. Micro-CT for Biological and Biomedical Studies: A Comparison of Imaging Techniques. J Imaging 2021; 7: 172. https://doi.org/10.3390/jimaging7090172

[54].de Lima IR, Costa AM, Bastos IN, et al. Development and characterization of 5% mol Zn bioceramic in granular form. Mater Res 2006; 9: 399–403. https://doi.org/10.1590/S1516-14392006000400010

[55].Yang Y, Yu H, Zhou X, et al. Shallow porous microsphere carriers with core-shell structure based on glass beads cross-linking chitosan for immobilizing inulinase. Mol Catal 2020; 486: 110871. https://doi.org/10.1016/j.mcat.2020.110871

[56].Senck, S., Glinz, J., Heupl, S., Kastner, J., Trieb, K., Scheithauer, U., Dahl, S. S., & Jensen, M. B. (2024). Ceramic additive manufacturing and microstructural analysis of tricalcium phosphate implants using X-ray microcomputed tomography. Open Ceramics, 19, 100628. https://doi.org/10.1016/J.OCERAM.2024.100628

[57].Dulgar-Tulloch AJ, Bizios R, Siegel RW. Human mesenchymal stem cell adhesion and proliferation in response to ceramic chemistry and nanoscale topography. J Biomed Mater Res A 2009; 90A: 586–594. https://doi.org/10.1002/jbm.a.32116

[58].Mealy J, O'Kelly K. Cell response to hydroxyapatite surface topography modulated by sintering temperature. J Biomed Mater Res A 2015; 103: 3533–3538. https://doi.org/10.1016/j.dental.2016.11.012

[59].Swain SK, Gotman I, Unger R, et al. Microstructure, mechanical characteristics and cell compatibility of β-tricalcium phosphate reinforced with biodegradable Fe-Mg metal phase. Epub ahead of print 2015. https://doi.org/10.1016/j.jmbbm.2015.09.002.

[60].Kang Y, Scully A, Young DA, et al. Enhanced mechanical performance and biological evaluation of a PLGA coated β-TCP composite scaffold for load-bearing applications. Eur Polym J 2011; 47: 1569–1577. https://doi.org/10.1016/j.eurpolymj.2011.05.004

[61].Khatiwala CB, Peyton SR, Metzke M, et al. The regulation of osteogenesis by ECM rigidity in MC3T3-E1 cells requires MAPK activation. J Cell Physiol 2007; 211: 661–672. https://doi.org/10.1002/jcp.20974

[62].Tsai SW, Liou HM, Lin CJ, et al. MG63 Osteoblast-Like Cells Exhibit Different Behavior when Grown on Electrospun Collagen Matrix versus Electrospun Gelatin Matrix. PLoS One 2012; 7: e31200. https://doi.org/10.1371/journal.pone.0031200

[63].Navarrete RO, Lee EM, Smith K, et al. Substrate Stiffness Controls Osteoblastic and Chondrocytic Differentiation of Mesenchymal Stem Cells without Exogenous Stimuli. PLoS One 2017; 12: e0170312. https://doi.org/10.1371/journal.pone.0170312